Geosciences

AIMS Geosciences, 12(1): 252–275.
DOI: 10.3934/geosci.2026010
Received: 28 September 2025
Revised: 22 December 2025
Accepted: 30 January 2026
Published: 02 March 2026

https://www.aimspress.com/journal/geosciences

Research article

Experimental and numerical studies of displacement fields and failure mechanisms in untreated and reinforced slopes using optical flow analysis

Gael Araujo[1,*], Mehrdad Razavi[1] and Jose R Zela[2]

[1] Department of Mineral Engineering, New Mexico Institute of Mining and Technology, 801 Leroy Place, Socorro, NM 87801, USA
[2] Department of Mining Engineering, West Virginia University, WVU, 1500 University Avenue, Stewart Hall, Morgantown, WV 26506-6201, USA

* **Correspondence:** Email: gaelestefany.araujohuaman@student.nmt.edu; Tel: (+1) 505 518 5041.

Abstract: Slope failures have caused significant human casualties and economic losses worldwide, with impacts reaching billions of dollars annually. These failures underscore the critical need for effective slope stability analyses. In particular, the mining industry faces this risk due to the accumulation of waste in tailing dams, which have a history of catastrophic failures. This study introduces a novel approach to analyze slope displacement fields and failure surfaces using the Digital Image Displacement (DID) method for an optical flow analysis, combined with a MATLAB code for data correction, numerical verification through Finite Element Method (FEM), and Limit Equilibrium Method (LEM) analyses. This novel methodology in geotechnical applications provides high, pixel-level sensitivity, thus enabling the detection of small displacement fields over short time intervals and spatially localized motions necessary to track the initial development of progressive failure. Forty-one experiments were conducted on untreated and geosynthetic-reinforced sandy slopes, thereby using more than 700 high-resolution digital images to investigate failure shapes and displacement fields. The results revealed a logarithmic spiral failure shape for both untreated and reinforced slopes, with reinforced slopes exhibiting deeper and more pronounced rupture surfaces. Geosynthetic reinforcement significantly improved the slope stability, which resulted in the Factor of Safety (FS) increase for 30° slopes from 1.2 to over 3 and increasing load-bearing capacity (up to 1700N) while reducing displacements. Additionally, the study emphasized the critical influence of slope geometry and compaction on the overall stability, thereby identifying closer reinforcement spacing (e.g., within one-third slope height) as the most effective design configuration to maximize stabilization. These findings offer valuable insights into the slope behavior, improve the precision of displacement measurements, and advance geotechnical engineering practices for enhanced risk mitigation and slope stability analyses.

Keywords: slope failure; digital image displacement; geosynthetic reinforcement; logarithmic spiral

1. Introduction

Slope failure events have triggered some of the most catastrophic scenarios globally, leading to human casualties, ecosystem affectation, and marine life death, which lead to both social and economic impacts. For instance, slope movements in countries such as Japan, Italy, the United States, and India resulted in billions of dollars in annual losses—US$ 4.5 billion in Japan, US$ 2.6 billion in Italy, US$ 2 billion in the United States, and US$ 1.5 billion in India [1–3]. Focusing deeper into the mining industry, this risk is also familiar with the slope failure effects, either in open pit failures or mostly in historic tailings dams failures such as the 1972 Buffalo Creek disaster [4], the 2000 Baia Mare spill [5], and the 2019 Brumadinho disaster [6], which resulted in substantial fatalities, machine losses, and the loss of millions of dollars. These catastrophic scenarios underscore the importance of an accurate slope stability analysis to mitigate these risks. A key component of a slope stability analysis is understanding the shape of potential failure surfaces, accurately assessing displacement field deformations, and finding new enhancing techniques to improve the slope stability.

Various traditional, numerical, mathematical, and unconventional methodologies have been developed in the literature to investigate the shape of critical failure surfaces in slopes [7–13]. These efforts aim to refine models to more accurately represent real-world conditions and enhance the precision of simulations. For example, advanced techniques such as the finite element method (FEM), particularly in Plaxis 2D and 3D, have shown that the damped sinusoidal shape more accurately represents critical slope failures compared to circular models. Mathematical models such as the brachistochrone curve, which is a cycloidal shape, have improved the computational efficiency to model sliding surfaces [9]. Despite extensive research on complex failure surface shapes, simplified models such as circular and logarithmic spiral slip surfaces are commonly adopted in engineering practice because they offer computational efficiency and robustness [14]. However, the impact of variations between these commonly used failure shapes on stability analyses remains uncertain.

As the slope stability remains a critical concern in geotechnical engineering, the use of geosynthetics to reinforce the soil and prevent slope failure has gained popularity. Geosynthetics improves the soil cohesion, thus reducing the likelihood of failure and increasing the overall strength of soil structures [15–17]. The effectiveness of geosynthetic reinforcement depends on factors such as the soil type, environmental conditions, spacing, and location. While many studies have documented the effectiveness of geosynthetics in increasing the Factor of Safety and load-bearing capacity, relatively few have analyzed the detailed failure shapes of reinforced slopes or systematically compared rupture surfaces between untreated and reinforced cases.

The interaction between geosynthetics and soil is another critical factor in slope stability. Multidirectional geosynthetics enhance the shear strength at the soil-geosynthetic interface due to the transverse ribs that resist deformation [13,15,17]. Although the localized frictional shear strength at this interface is often technically lower than that of the soil's internal shear strength, geosynthetics significantly enhance the overall slope stability [17]. This enhancement is achieved by providing mechanical interlocking with soil particles, efficiently distributing loads, and limiting deformation while reducing the stress concentration. Furthermore, the strength can be improved by optimizing the soil properties, such as utilizing larger soil particles and higher sand densities to enhance the stability through increased friction and adhesion [16]. Additionally, research has demonstrated that the vertical spacing of geosynthetic layers plays a significant role in reinforcing slopes, with closer spacing and more layers improving the safety factors [18].

The development of advanced imaging technologies, such as Digital Image Correlation (DIC) and Particle Image Velocimetry (PIV) [19,20], has significantly advanced our understanding of the slope behavior, failure mechanisms, and particle behavior at the geogrid interface. DIC and PIV capture high-resolution images before and after deformation to measure displacements and strains with a sub-pixel accuracy through cross-correlation [21,22]. In the context of laboratory-scale slope monitoring, DIC and PIV are generally capable of capturing deformations with high precision. However, its subset-based formulation can limit the sensitivity to very small, highly localized, and incremental displacements that occur over short time intervals, particularly when these motions only involve a few grains or approach the lower bounds of sub-pixel resolution. As a result, the earliest stages of slope failure may not be fully resolved.

Recent improvements in camera resolution and image processing algorithms have further enhanced the accuracy and efficiency of emerging imaging techniques, such as Digital Image Displacement (DID), applied here for the first time in geotechnical studies, while also reducing the computational time [23] and dependence on specialized software or acquisition systems.

DID, which is based on optical-flow analysis, overcomes these limitations by computing displacement at the pixel level using the brightness constancy assumption between consecutive frames. This pixel-wise formulation allows for the detection of subtle, continuous, and spatially localized motions without the need for correlation of subsets. Consequently, DID is particularly well-suited to track the initial development of deformation and the progressive formation of failure surfaces. By analyzing consecutive images at short temporal intervals, DID provides a high-resolution representation of displacement evolution across the slope, thus enabling a clear empirical characterization of the transition from a stable state to failure. Its pixel level sensitivity and ability to resolve incremental motions make DID the primary technique used in this study. This study highlights the existing gaps in understanding the slope behavior. It aims to explore the failure shapes of untreated and reinforced slopes under loading conditions in dry environments by capturing the evolution of the slope deformation from its static to its failure state. The research employs a DID technique using Mathematica's Wolfram language, thus pioneering its application in geotechnical engineering.

2. Materials and methods

2.1. Material characterization and properties

2.1.1. Soil characterization

The study utilized a Poorly Graded Coarse Sand classified according to the Unified Soil Classification System (USCS). Grain Size Distribution (GSD) tests indicates that nearly the entire 500 g soil sample (499 g) was retained on sieve No 20 (0.85 mm), with only about 0.1 g retained on sieve No. 60 (0.25 mm) (Figure 1a and 1b). The sand particles range from 1 mm to 1.2 mm, with shapes varying from sub-angular to sub-rounded (Figure 1c). These results confirm that the sand used is highly uniform.

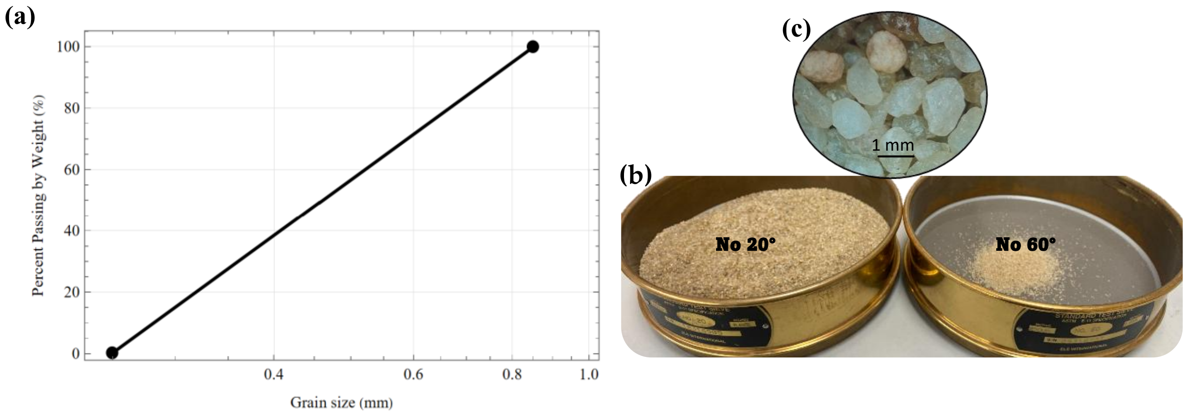

Figure 1. (a) Grain size distribution curve, (b) Sand sample in sieves, (c) Sand grains particles.

Geomechanical characterization via direct shear tests (ASTM D-3080) revealed that the sand under vertical loads of 400N, 1200N, and 3600N exhibited a friction angle (ϕ) of 37° and a cohesion (c) of 0.069 N/mm² (Figure 2). This friction angle is typical for medium-dense to dense sands and was used to determine the experimental slope angles.

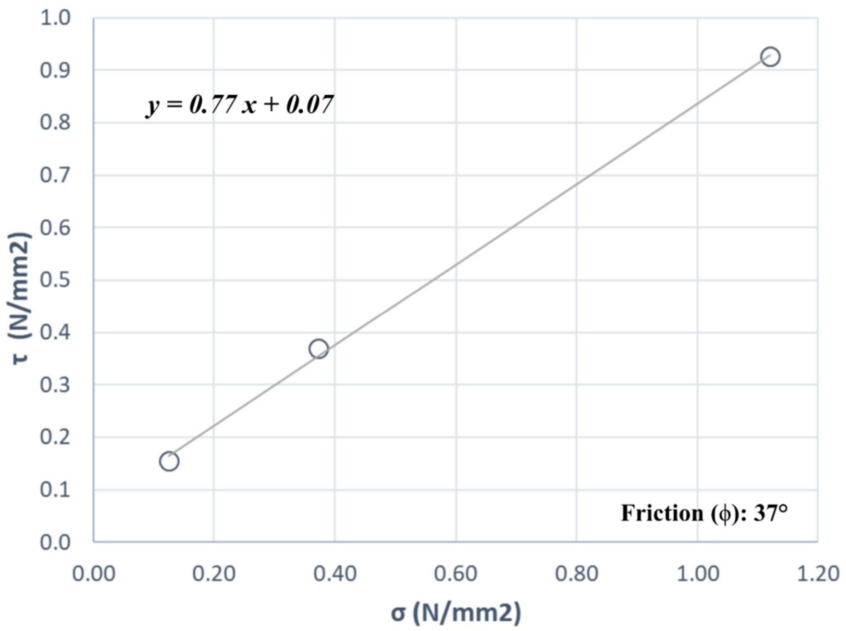

Figure 2. Normal stress vs Shear stress.

2.1.2. Geosynthetic characterization

The reinforcement material is a polypropylene geosynthetic-like net extracted from a commercial turf reinforcement mat system (VMAX P550_ ISO 10318). This three-dimensional geosynthetic consists of a UV-stabilized polypropylene fiber matrix. As the extracted net is not a standalone commercial product, because it is a small-scale compared to the actual VMAXP550 with a thickness of 1.8 cm, manufacturer-certified tensile properties are not available. For reference, the VMAX P550 has a tensile strength of 21.1 kN/m in the machine direction and 17.7 kN/m in the transverse direction, thus providing grid-like mechanical interlocking with the soil. However, because the extracted net is of a smaller scale, its mechanical properties are significantly lower. Therefore, the numerical modeling in this study employed reduced elastic stiffness parameters (scaled stiffness) to accurately reflect the behavior of the reinforcement at the laboratory scale. This approach ensures that the numerical analysis captures the relative reinforcing effect and deformation patterns observed in the small-scale experiments, rather than attempting to replicate the absolute stiffness of the full-scale product.

Due to the small scale of the available direct shear box (6.3 cm diameter), the experimental program was not extended to directly measure the interface friction between the coarse sand and the geosynthetic. However, according to research by Liu et al., while the localized frictional shear strength at such interfaces may technically be lower than the soil's internal shear strength, the inclusion of geosynthetics significantly enhances the overall slope stability [17]. This improvement is achieved by optimizing the load distribution, providing mechanical interlocking, and reducing localized failure zones. The performance of these reinforcements is further influenced by factors such as rib strength and specific soil-particle interactions [12,15–17].

2.2. Experimental instrumentation and boundary conditions

The experimental setup evolved through three stages to improve the structural stiffness and address boundary effects. These refinements ensured that the physical model could eliminate deformation of the model containers and withstand higher loads so they can provide accurate data for the optical flow analysis.

2.2.1. Physical model containers

The choice of testing containers significantly evolved to eliminate deformation of the box itself:

- Stage 1 (Initial Testing): A transparent acrylic box (50 cm L × 35 cm H × 9 cm W) with a 3 mm wall thickness was used (Figure 3a). This box proved structurally inadequate, exhibiting bending and cracking under high loads, thus preventing it from sustaining the loading levels achieved in later stages.
- Stages 2 and 3 (Improved design box): Employed a robust polycarbonate box (55 cm L × 30 cm H × 10 cm W) with a 10 mm wall thickness and an external wooden frame (Figure 3b), thus providing significantly greater stiffness to prevent container deformation during the experiment.

2.2.2. Loading process

The method of applying vertical compression was upgraded to ensure precision and control:

- Stages 1 and 2: Loading was manually performed using 1 kg and 4 kg weights added in discrete increments (Figure 3a and 3b).
- Stage 3: The setup was upgraded to a mechanized, quasi-static system. The polycarbonate box was integrated between two Versa Loader frames configured to act as a single unit (Figure 3c).

This system allowed for uniform uniaxial compression applied at 5-second intervals, thus avoiding dynamic effects. To ensure a uniform distribution of forces, a wooden square piece was placed at the top of the slope, serving as a flat interface between the loading frame and the soil surface (see Figure 5). The Versa Loader enabled a more controlled load, and images were acquired after stabilization at each increment.

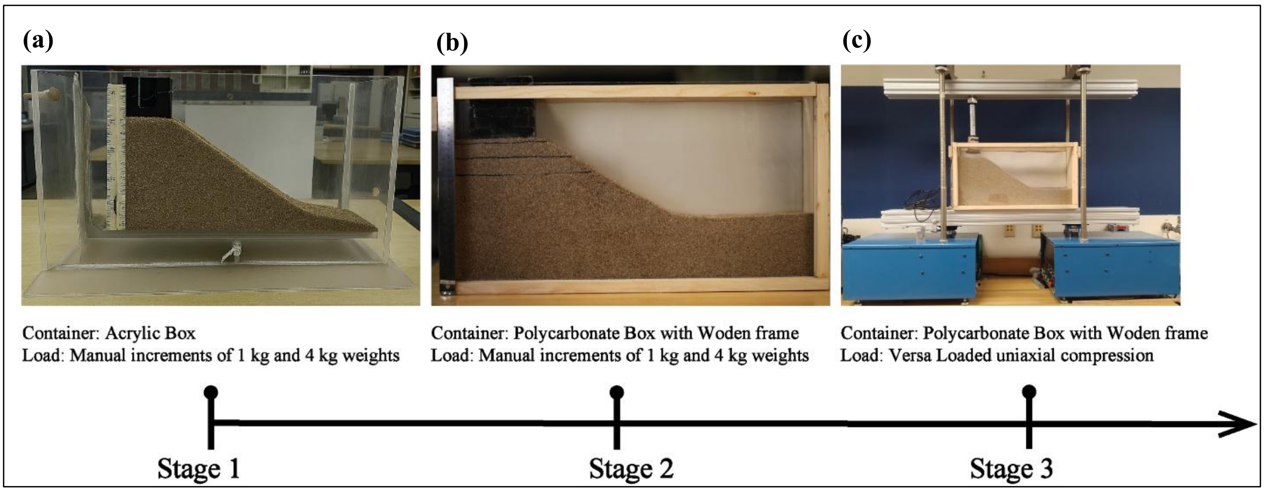

Figure 3. Evolution of experimental instrumentation. (a) Stage 1, (b) Stages 2, (c) Stage 3.

2.2.3. Imaging systems

The imaging setup remained consistent and precise throughout the stages.

A Canon EOS 5D Mark II (21-megapixel sensor) was mounted on a leveled tripod to prevent distortion. Additionally, adjustable studio lights were used to maintain the brightness constancy, which is a crucial assumption for optical flow analysis, thus ensuring that the pixel intensities remained unchanged between consecutive frames except for motion.

2.2.4. Boundary effect observation

The limited width of the model containers (9–10 cm) necessitated a careful evaluation of the boundary effects, particularly as the increased load-bearing capacity in Stage 3 intensified the soil–geosynthetic–sidewall interaction. Visible abrasion and scratching on the polycarbonate walls during loading confirmed the mobilization of grain–wall friction. Laboratory measurements determined the friction angle between the polycarbonate sidewall and the sand was 21°, while the sand's internal friction angle was 37°. Because the internal shear strength of the soil was substantially higher than the interface friction of the container, the internal failure mechanisms remained the primary drivers of the slope behavior.

2.3. Experimental design and model construction

To address the study's objectives, the experimental program was divided into two primary categories: untreated slopes (17 tests) and geosynthetic-reinforced slopes (24 tests). This division allowed for a direct comparison of displacement fields and failure mechanisms.

2.3.1. Model geometry

Slopes were constructed at 30° and 35° angles. The 35° angle was selected to simulate near-critical conditions close to the soil's angle of repose (37°), while the 30° angle served as a conservative baseline. To ensure consistency across the test in different stages, a wooden mold was used to shape the slopes within the boxes. To further guarantee the precision of the slope inclinations (30° and 35°), a digital protractor was utilized to verify the final angle after molding, thus ensuring highly repeatable and accurate geometries for all 41 tests.

2.3.2. Compaction protocols

To ensure repeatable initial conditions, the slopes were built in three compacted layers, with each layer receiving 24 hammer tamps from a 20 cm drop height. This compaction level resulted in a relative density of aproximately 58% compaction, calculated using a maximum void ratio (e max) of 0.75, a minimum void ratio (e min) of 0.56, and a measured void ratio (e) of 0.64 obtained from laboratory results.

A preliminary test indicated that a lower compaction (10–20 tamps) resulted in “loose soil” behavior where compression curves failed to reach a peak, while a higher compaction (30 tamps) increased loads beyond the safe operational limits of the testing containers. Consequently, the 24-tamp compaction level was selected as a balanced condition, thus ensuring the formation of well-defined failure surfaces suitable for an optical flow analysis, while simultaneously preventing the bending or cracking observed in the Stage 1 box design.

2.3.3. Geosynthetic placement and spacing

In reinforced experiments, three layers of VMAX P550 Turf Reinforcement Mat, with square apertures of approximately 1 cm × 1 cm between ribs and thickness of 2 mm (Figure 4a) were installed to identify the most effective stabilization configuration. The reinforcement layers were equally spaced within the upper one-third, two-fifth, and one-half of the total slope height (H = 22 cm for 30° slopes and H = 24 cm for 35° slopes). To maintain a high geometric repeatability across all tests, a custom wooden mold was positioned at the top of the testing box during construction, thus ensuring that the slope geometry and geosynthetic alignment remained consistent despite the narrow 9 cm and 10 cm boxes width.

The experimental findings identified that reinforcement within the upper one-third (1/3) of the slope height as the most effective design to maximize the load-bearing capacity and reduce displacement. However, this configuration also presented the greatest construction challenges; at this spacing, the gap between the soil-geosynthetic system and the lateral walls was locally less than 2 cm. This constrained geometry intensified the soil-geosynthetic-sidewall interaction, contributing to the grain-wall friction observed through surface scratching on the polycarbonate.

To ensure precision during the mechanized loading in Stage 3, the reinforcement layers were installed at the following exact vertical spacings (Figure 4b):

- For 30° slopes, the reinforcement layers were spaced approximately 2.4 cm within the upper one-third (1/3) of the slope height, 2.7 cm within the upper two-fifths (2/5), and 3.6 cm within the upper one-half (1/2). For 35° slopes, the corresponding spacings were approximately 2.6 cm, 3.2 cm, and 4.0 cm within the same respective zones of the slope height.

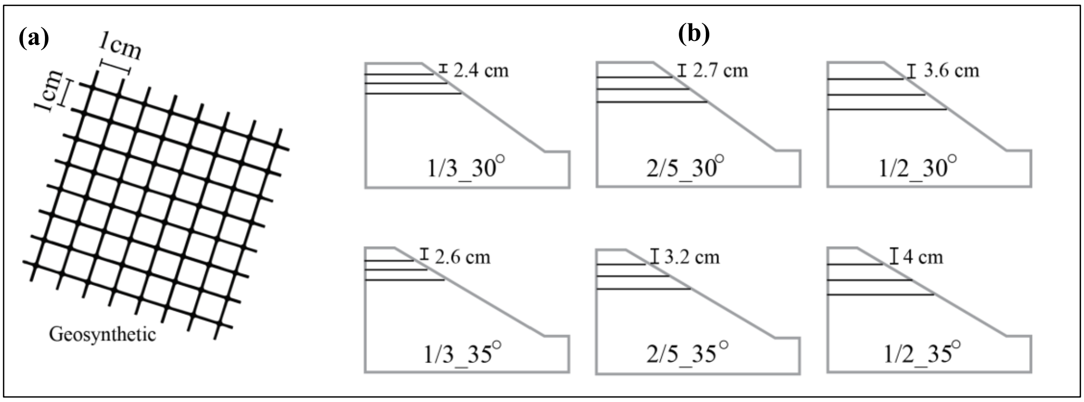

Figure 4. (a) Geosynthetic aperture. (b) Geosynthetic location and spacing at 30° and 35° at one-third (1/3), two-fifth (2/5), and one-half (1/2) slope height.

2.4. Data analysis and methodology

The methodology transitions from the physical laboratory stages described in 2.2 and 2.3 to an advanced digital analysis and numerical verification. The central focus of this research is the pioneering application of the DID method, which serves as the primary tool to identify failure surfaces and quantify displacement fields.

2.4.1. Data Acquisition

The experimental program generated a comprehensive dataset of over 700 high-resolution images from 41 tests. These images captured the complete evolution of the slopes from a static state to a failure state (Figure 5). The resolution was maintained at a high standard to support a pixel-wise analysis: 5616 × 3744 pixels for Stages 1 and 2, and 4080 × 2720 pixels for Stage 3.

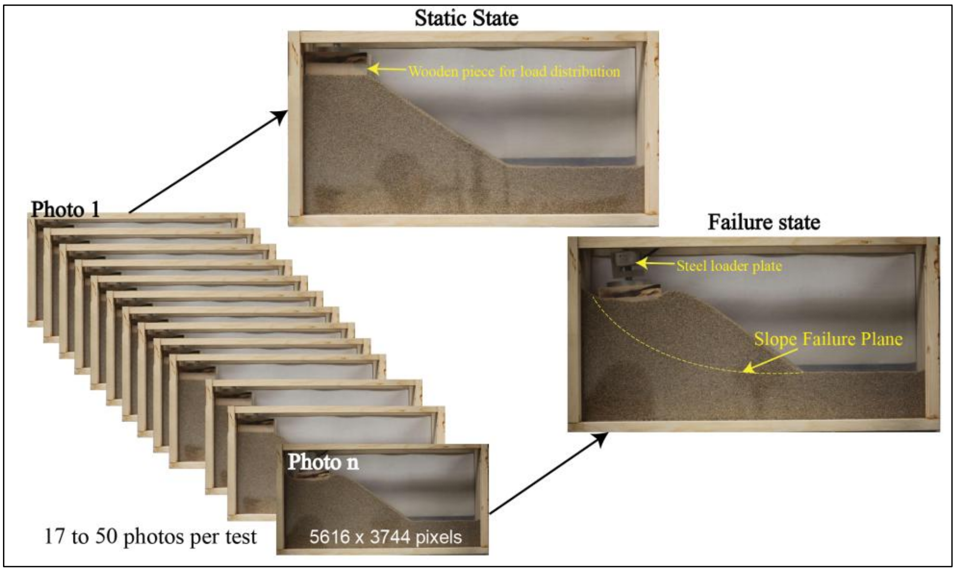

Figure 5. Sequence of high-resolution images capturing slope failure progression.

2.4.2. Primary methodology: Digital image displacement (DID)—optical flow method

The DID method is the primary technique used to characterize the transition from stable states to failure. Unlike subset-based methods such as DIC, which can be limited by the size of their tracking windows, the DID method calculates displacement at the individual pixel level to achieve a high sensitivity.

- Pre-processing and Cropping: Before the DID comparison, high-resolution photos were cropped using the Wolfram Mathematica software to exclusively focus on the box window (Figure 6). This removes irrelevant background details, ensures that the images have identical dimensions, and enhances the processing efficiency.
- Displacement Computation: The core calculation was performed using the Wolfram Language command flow = ImageDisplacements[{DI(1), DI(2)}]. This algorithm utilizes Farneback and Dense Inverse Search algorithms to compute horizontal (δx) and vertical (δy) displacement matrices between two consecutive photos [24] (Figure 6). The process relies on the brightness constancy assumption, which assumes that the pixel intensities remain unchanged except for motion, thus allowing the software to detect subtle, grain-by-grain movements. This process was repeated multiple times to compare consecutive images and compute the cumulative total displacement, as each test includes between 17 and 50 photographs, spanning from the initial static state to the final failure state (Figure 5).
- Initial Rescaling (Mathematica): Once the pixel comparison is complete, the data underwent an initial rescaling process using the code Image /@ Rescale /@ flow. This step generated a displacement field visualization where all values are normalized to a range between 0 and 1. In this representation, 0 (shown in purple) indicates no displacement, while 1 (shown in green) corresponds to the maximum displacement observed between the two images (Figure 6).
- Final Scaling (MATLAB): To translate these digital results into physical measurements, the matrices were exported to MATLAB for final processing. This stage involved a physical scaling, thereby converting the 0–1 pixel values into actual displacements in millimeters (mm) based on the physical model dimensions. The final DID results displayed displacement fields using a color gradient, where blue represents 0 mm and yellow represents the maximum displacement (typically <3 mm), see Figure 6.

It is important to note that the DID results represent incremental deformation rather than cumulative totals. Because images were acquired at 5-second intervals during the quasi-static loading process, the method captures the subtle, high-resolution evolution of displacement between the individual steps, thus enabling a clear characterization of the progressive formation of failure surfaces

2.4.3. Reliability and numerical verification

To ensure the scientific validity and reliability of the novel DID findings, the following secondary numerical methodologies were employed:

- FEM (Plaxis 3D): Finite Element Method simulations were used to validate the experimental results, thereby ensuring that the displacement fields observed through the camera aligned with theoretical soil-structure interaction models.
- LEM (Slide 2D): The Limit Equilibrium Method (LEM) was used to calculate the Factor of Safety (FS). Crucially, the failure surfaces identified by the DID method were used as the

primary reference for these calculations, thus providing empirical grounding for the numerical stability analysis.

To provide a clear roadmap of the research logic, a Methodology Workflow (Figure 6) illustrates the structured approach used throughout the study. This workflow highlights the centrality of the DID method in identifying the failure mechanisms, followed by image-rescaling and final verification through FEM validation and LEM-based safety factor calculations.

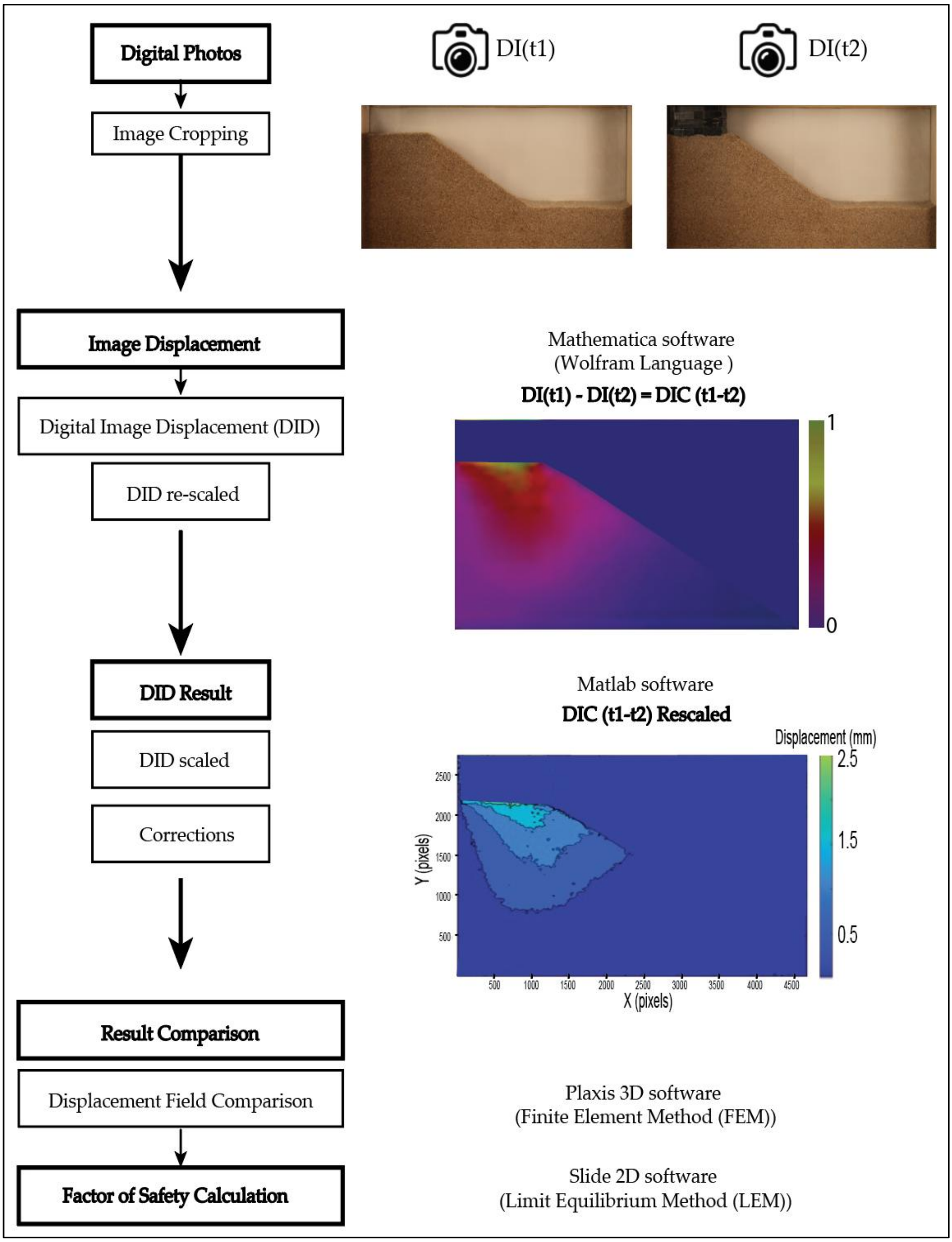

Figure 6. Methodology workflow.

3. Results

3.1. Untreated slopes analysis

3.1.1. Uniaxial compression test results

The uniaxial compression test results for untreated slopes, conducted in stage 3 of the experiment, provide insights into the load-bearing behaviors of slopes at 30° and 35° angles. The experimental setup incorporated force and displacement sensors at the top and bottom of the Versa Loaders, thus ensuring precise force measurement (in Newtons) and vertical displacement (in millimeters) during compression. The 30° slopes supported a maximum load range from 679 to 710 N. In comparison, the 35° slopes supported loads between 598 N and 628 N. Notably, the slope angle influenced load-bearing capacity, with 30° slopes exhibiting a greater load tolerance. The failure vertical displacement for the 30° slope ranged between 8 mm and 9 mm, while the 35° slope failed between 6 mm and 7 mm, as depicted in Figure 7.

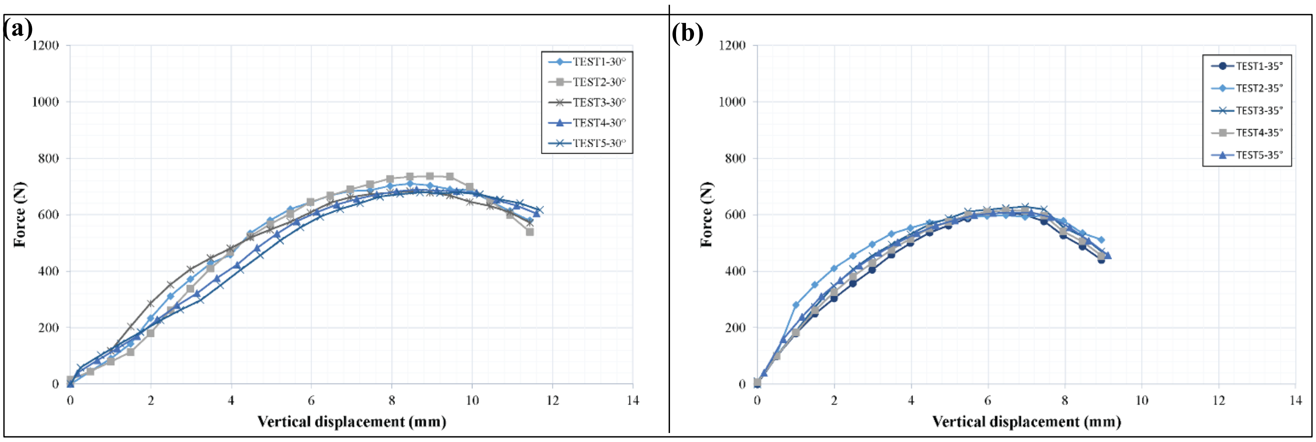

Figure 7. Force versus vertical displacement in untreated slopes for a slope angle of (a) 30° (b) 35°.

3.1.2. Digital image displacement (DID) results

Seventeen experiments were analyzed using manual and automatic load application methods, with the DID technique employed to calculate displacement from static to failure conditions. This approach provides insight into the evolution of displacement fields and failure shapes as the load is progressively applied. In Stage 1, experiments conducted in a 0.3 mm-thick acrylic box showed displacement values ranging from 3.3 mm to 3.7 mm for 30° and 35° slopes, with maximum support loads of 314 N and 383 N, respectively. In Stage 3, using more robust setups, the 30° slopes exhibited displacements between 4.05 mm and 4.80 mm, with failure loads ranging from 679 N to 736 N. For the 35° slopes, the displacements ranged from 4.75 mm to 4.98 mm, with the failure loads varying from 598 N to 628 N. Figure 8 shows the DID results for Tests 1 of Stage 3, depicting untreated 30° and 35° slopes. Additionally, the results summarized in Table 1 demonstrate consistent failure displacement patterns for untreated slopes.

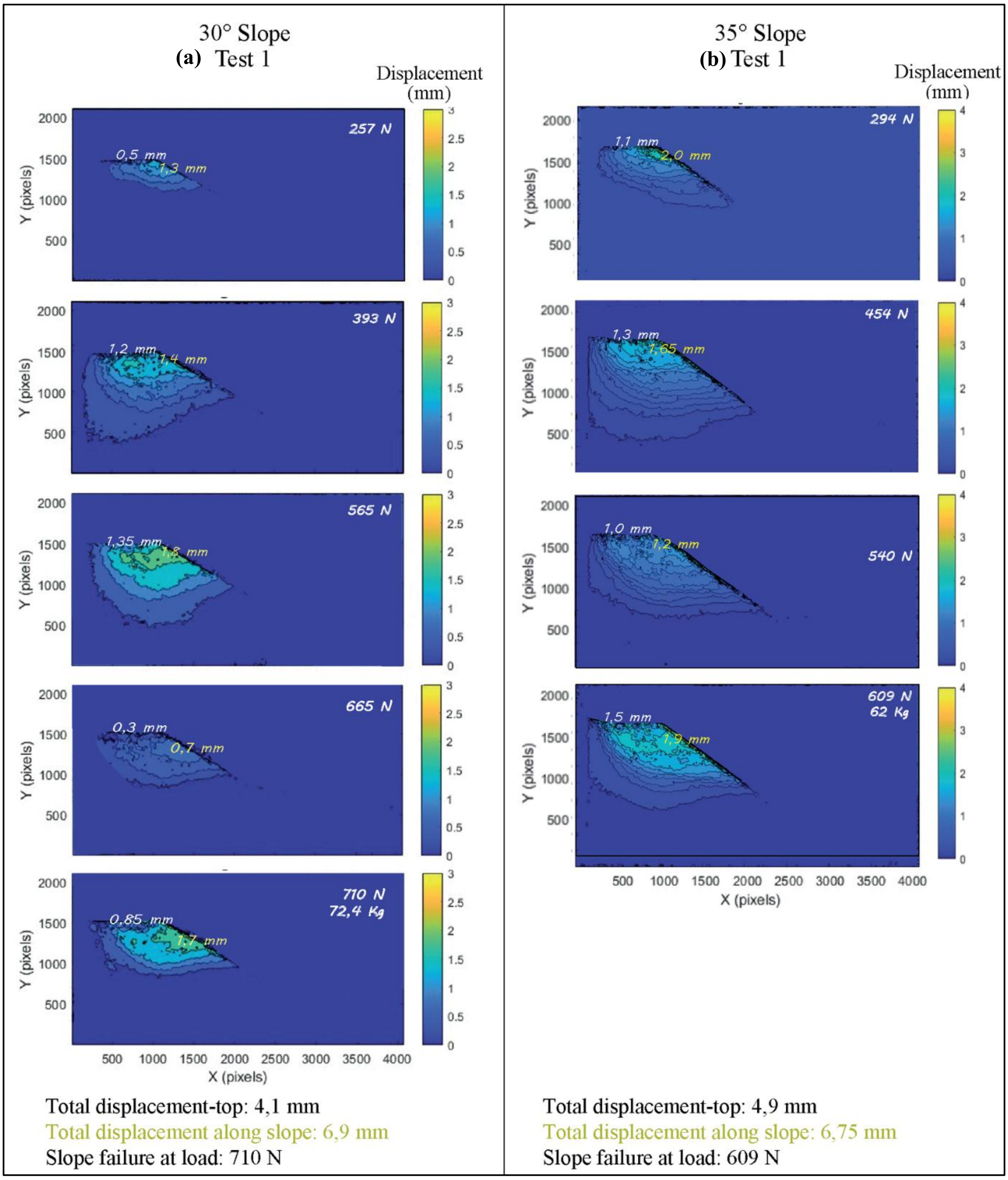

Total displacement-top: 4,1 mm
Total displacement along slope: 6,9 mm
Slope failure at load: 710 N

Total displacement-top: 4,9 mm
Total displacement along slope: 6,75 mm
Slope failure at load: 609 N

Figure 8. Displacement fields and shape failure evolution of untreated slopes with DID technique (a) 30° and (b) 35°.

3.1.3. Displacement field comparison: DID vs. PLAXIS 3D

The displacement field obtained from the DID technique closely aligns with PLAXIS 3D simulations, where the numerical model was specifically scaled to the laboratory configuration rather than a full-scale field application. To ensure consistency with the experimental dimensions, boundary conditions, and low stress levels, the soil was modeled using an elastic-perfectly plastic Mohr-Coulomb constitutive model, and the VMAX P550 geosynthetic was assigned reduced axial and shear stiffness values (EA1 = 5.034 N/mm, EA2 = 5.833 N/mm, and GA = 2.240 N/mm). These parameters were intentionally selected to capture the relative reinforcing effect and ductile deformation patterns observed at the laboratory scale rather than the absolute stiffness of the full-scale product. For untreated slopes at 30° and 35° under failure loads of 710 N and 609 N, the DID-measured displacements of 4.2 mm and 4.9 mm demonstrated a strong correlation with the simulated values of 4.1 mm and 4.45 mm, respectively (Figure 9). This alignment validates the precision of the DID method and confirms that the scaled numerical model effectively reproduces the physical failure mechanisms observed in the testing box.

Table 1. Maximum Load of failure and DID displacement fields for untreated slopes.

Angle (°)	Weight (N)	Max Force (N)	DID Total Displacement at the top (mm)	Cropped image Dimensions	Instrumentation Set Up Stage
30	383	383	3.70	{3812, 2347}	Stage 1
30	363	363	3.50	{5616,3495}	
30	373	373	3.60	{5616,3495}	
30	710	710	4.10	{4080, 2101}	test1 Stage 3
30	736	736	4.80	{4080, 2101}	test2
30	683	683	4.75	{3702, 1992}	test3
30	689	689	4.60	{4069, 2150}	test4
30	679	679	4.05	{4071, 2101}	test5
33	314	314	3.30	{5302, 2632}	Stage 1
33	304	304	3.40	{5132,3271}	
34	275	275	3.50	{3812, 2347}	
35	167	167	3.45	{3812, 2347}	
35	196	196	3.50	{5616,3495}	
35	186	186	3.60	{5615,3494}	
35	609	609	4.90	{4076, 2162}	test1 Stage 3
35	598	598	4,75	{4080, 2172}	test2
35	628	628	4.98	{4071, 2177}	tets3

3.2. Reinforced slopes analysis

The reinforced slopes at 30° and 35° angles incorporated geosynthetic layers equally spaced within varying zones of the slope height at one-third (1/3), two-fifths (2/5), and one-half (1/2). These configurations demonstrated maximum loads ranging from 1250 N to 1700 N for 30° slopes and from 929 N to 1171 N for 35° slopes (Figure 10). These maximum loads for reinforced slopes were consistently higher than those observed for untreated slopes, thus highlighting the reinforcing effect of the geosynthetics. The analysis revealed a clear improvement in load-bearing capacity for the reinforced slopes compared to the untreated ones. Lower slope angles further enhanced the stability, providing even more resistace to failure than the higher slope angles.

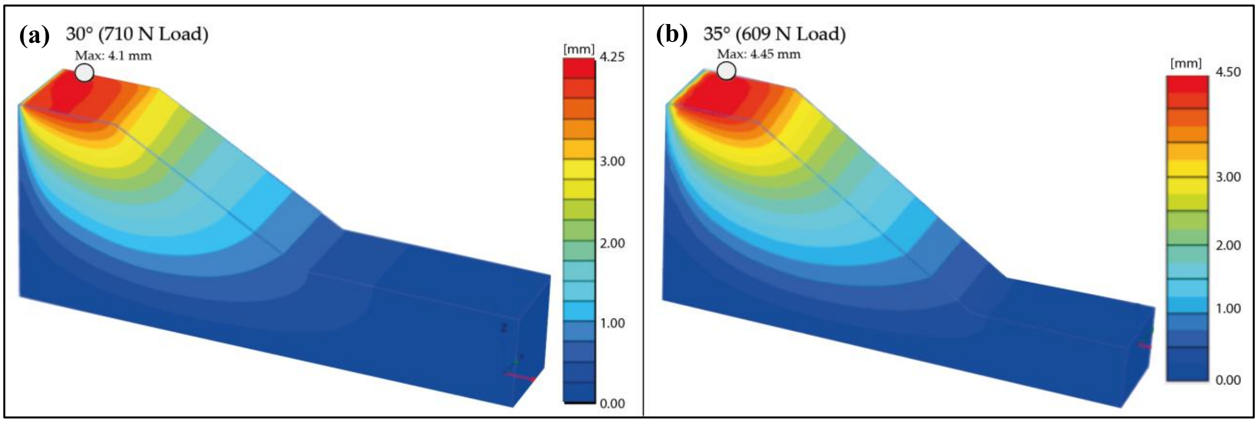

Figure 9. Numerical modeling of untreated slopes in PLAXIS 3D. (a) Slope angle = 30°, (b) Slope angle = 35°.

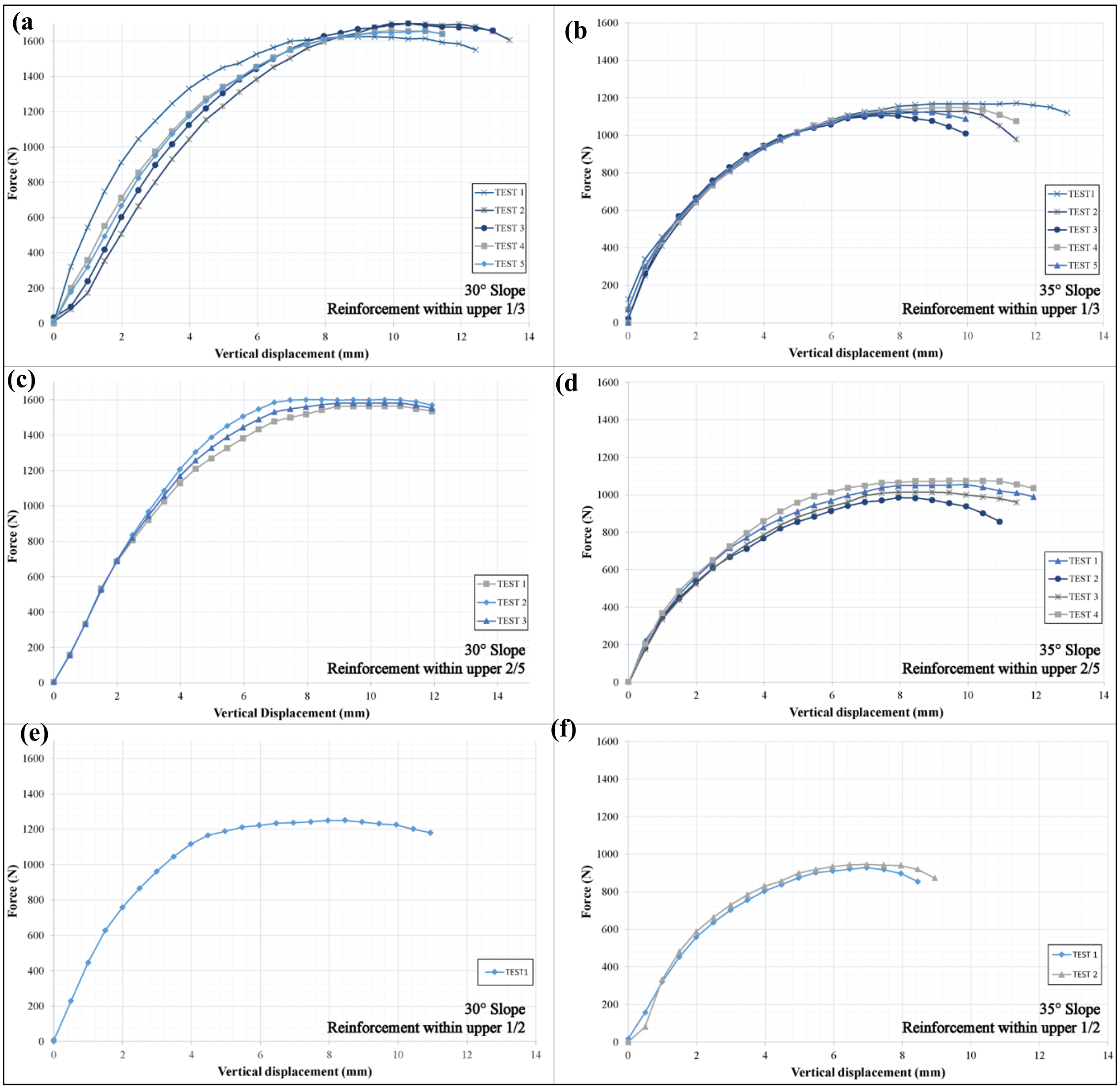

Figure 10. Load displacement response during compression tests on reinforced slopes at 30° and 35°. Each slope was reinforced with three geosynthetic layers, spaced equally, within slope heights of: (a,b) One-third (1/3), (c,d) two-fifths (2/5), and (e,f) one-half (1/2).

3.2.1. Digital image displacement (DID) results for reinforced slopes

For reinforced slopes at 30° and 35° angles, Stage 1 experiments revealed total displacement fields ranging from 3.3 mm to 3.5 mm, with maximum support loads of 216 N and 334 N for two-thirds spacing. In Stage 2, the total displacement increased to 5.4–5.5 mm, with a maximum support load of 706 N at one-half spacing. For two-thirds spacing in this stage, the displacement ranged from 5.75 mm to 5.9 mm, with maximum loads of 677 N and 687 N for reinforced slopes at 30° and 35°.

In Stage 3, the total displacements for reinforced slopes at 30° ranged from 6.2 mm to 7.4 mm, with loads varying from 1250 N to 1700 N. For 35° slopes, the displacements ranged from 5.1 mm to 7.0 mm, with loads ranging from 929 N to 1171 N (Table 2), when three geosynthetic layers were placed within one-half, two-fifths, and one-third of the total slope height (Figure 11).

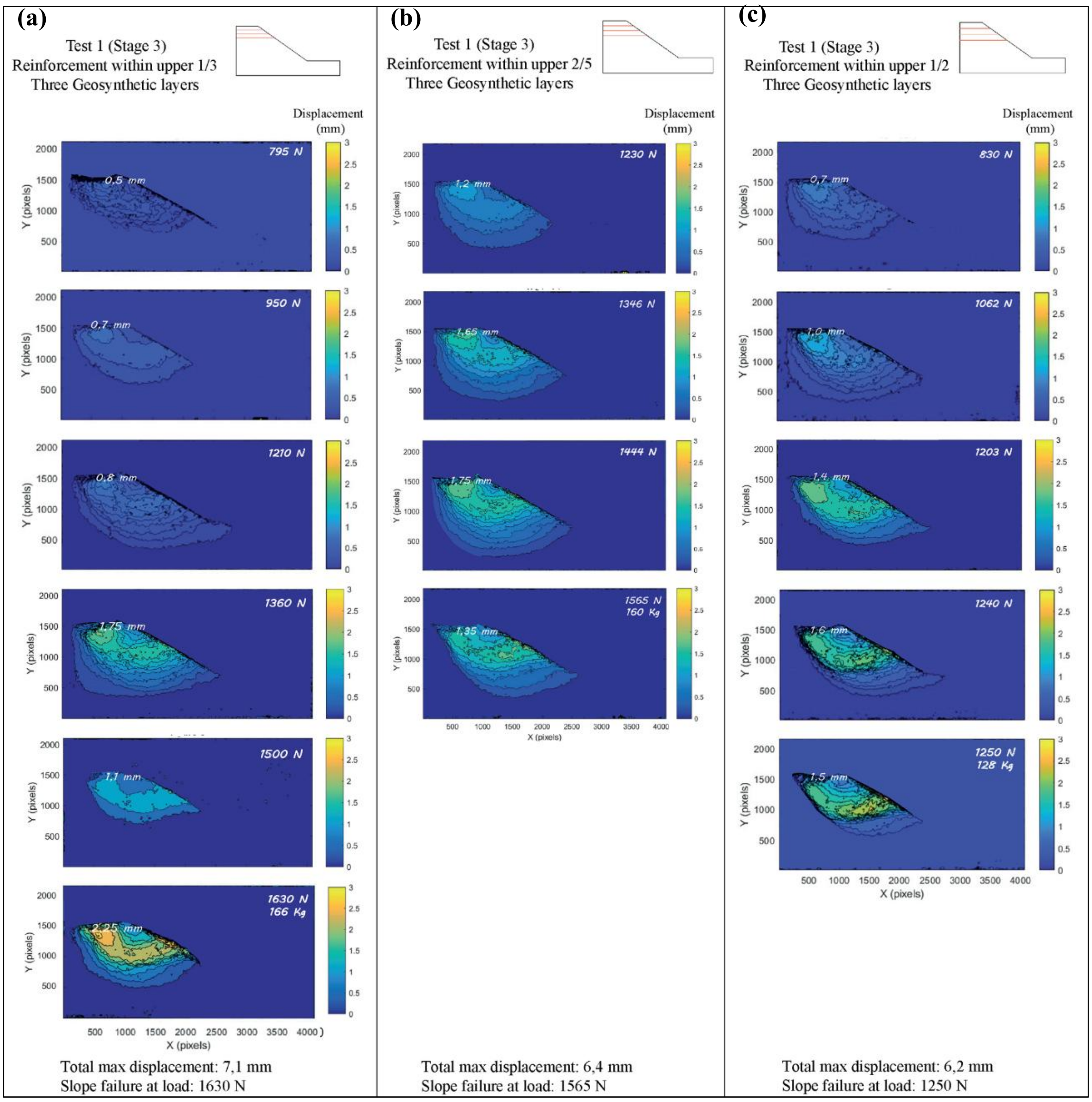

Figure 11. DID displacement fields evolution on reinforced 30° slopes with three geosynthetic layers, spaced equally, within slope heights of (a) one-third, (b) two-fifth, and (c) one-half.

As the geosynthetic spacing decreased, the slope could support higher loads. The displacement behavior for the reinforced slopes exhibited reduced bulging compared to untreated slopes, thus highlighting the improved overall stability provided by the geosynthetic reinforcement. Additionally, while the total displacement fields for the 30° and 35° slopes improved the overall stability, it is noteworthy that the reinforced slopes at 35° supported lower loads compared to those at 30°.

Table 2. Failure loads and DID displacement fields for reinforced slopes.

Angle (°)	Weight (N)	Slope height	Number of Geosynthetic Layers	Max Force (N)	Total Displacement (mm)	Trim image Dimensions	Instrumentation Set Up Stage
30	284	2/3	3	284	3.30	{5616, 3445}	Stage 1
30	334	2/3	3	334	3.50	{5616, 3600}	
30	706	1/2	3	706	5.40	{5527, 3042}	Stage 2
30	687	2/3	3	687	5.90	{5527, 3042}	
30	1630	1/3	3	1630	7.10	{4080, 2101}	test Stage 3
30	1700	1/3	3	1700	7.40	{4076, 2151}	test
30	1699	1/3	3	1699	7.10	{4080, 2181}	test
30	1565	2/5	3	1565	6.40	{4031, 2151}	test
30	1600	2/5	3	1600	6.53	{4080, 2181}	test
30	1250	1/2	3	1250	6.20	{4073, 2151}	test
35	216	2/3	3	216	3.10	{5620, 3445}	Stage 1
35	226	2/3	3	226	3.20	{5624, 3449}	
35	706	1/2	3	706	5.50	{5527, 3042}	Stage 2
35	677	2/3	3	677	5.75	{5527, 3042}	
35	687	2/3	3	687	5.80	{5247, 2502}	
35	1171	1/3	3	1171	7.00	{4080, 2162}	test Stage 3
35	1127	1/3	3	1127	5.85	{4051, 2162}	test
35	1105	1/3	3	1105	5.80	{4061, 2162}	test
35	985	2/5	3	985	5.35	{4076, 2181}	test
35	1054	2/5	3	1054	5.55	{4076, 2181}	test
35	1014	2/5	3	1014	5.55	{4076, 2181}	test
35	1075	2/5	3	1075	5.65	{4080, 2181}	test
35	929	1/2	3	929	5.10	{4076, 2162}	test
35	945	1/2	3	945	5.40	{4056, 2162}	test

3.2.2. Displacement field comparison: DID vs. PLAXIS 3D for reinforced slopes

A comparison between the DID and PLAXIS 3D results for reinforced slopes at different geosynthetic spacings revealed small discrepancies in the displacement values. For instance, at a load of 1630 N under the configuration where the reinforcement layers were equally spaced within the upper one-third (1/3) of the slope height, the DID method measured 7.1 mm, while PLAXIS 3D simulated 7.68 mm (Table 3). These slight differences are specifically attributed to the limitations of scaling prototype material properties to a narrow 10 cm box environment, where intensified grain–wall friction was mobilized, as evidenced by visible scratching on the polycarbonate walls. Despite these small-scale boundary effects, the close alignment confirms that the scaled elastic stiffness properties (EA and GA) successfully captured the ductile deformation behavior of the reinforced soil mass.

Table 3. Maximum displacements-comparison between DID and PLAXIS 3D.

Load (N)	Slope Heights	DID (mm)	PLAXIS 3D (mm)
1630	One-third	7.1	7.68
1565	Two-fifth	6.4	7.36
1250	One-half	6.2	6.02

3.2.3. Calculation of the Safety Factors

The results highlight a significant improvement in the slope stability when geosynthetic reinforcement was applied, particularly when layers are distributed within the upper one-third (1/3) of the slope height. For example, for 30° slopes under a 710 N load, the FS increased from 1.2 (untreated under load) to 3.12 (Figure 12), thus representing a 160% stability gain. Similarly, for 35° slopes under a 690 N load, the FS improved from 1.02 to 2.67, thereby achieving a 162% gain and validating geosynthetics as a critical risk mitigation technique even for geometries near the soil's 37° angle of repose.

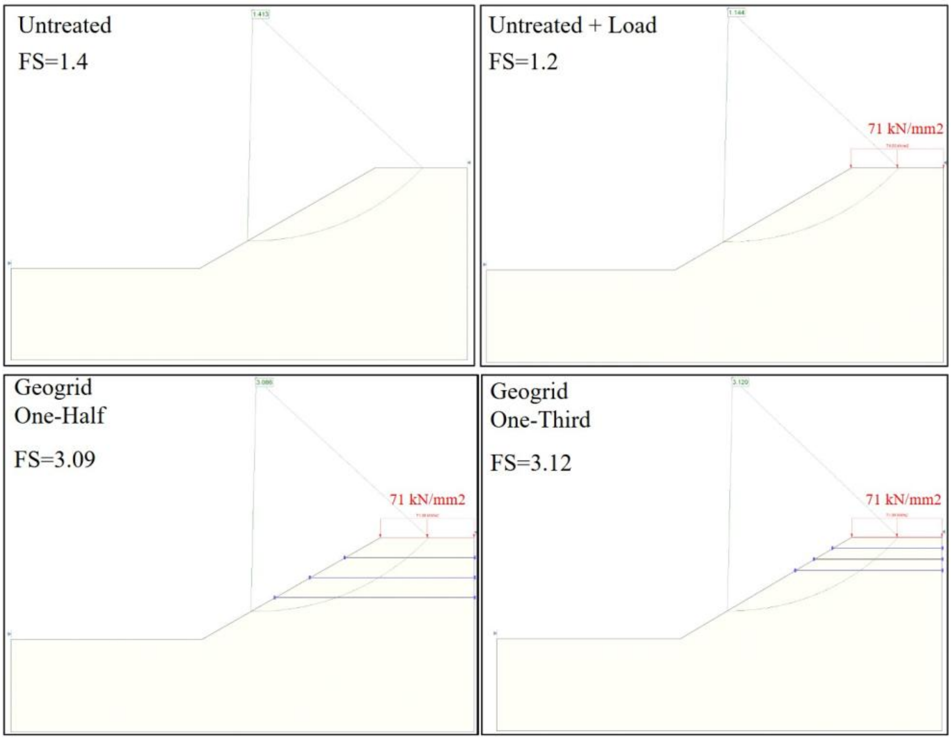

Figure 12. Factor of safety under untreated and reinforced slopes at 710N–30°.

4. Discussion

4.1. Maximum load supported by untreated and reinforced slopes

Untreated 30° slopes supported an average load of 700 N, while untreated 35° slopes displayed a lower capacity of 600 N. Geosynthetic reinforcement significantly enhanced the load-bearing capacity of both slope types. For 30° slopes, the maximum load at the peak of the load-displacement curve substantially increased when three reinforcement layers were distributed within the upper one-third (1/3) of the slope height supporting 1700N, within two-fifths (2/5) supporting 1582 N, and within one-half (1/2) supporting 1250 N. These results confirm that closer geosynthetic spacing enhances the load distribution and slope stability. However, for 35° slopes, the maximum loads were lower, with values of 1171 N, 1032 N, and 929 N for the reinforcement layers distributed within upper one-third (1/3), two-fifths (2/5), and one-half (1/2) slope height, respectively (Figure 13). These findings indicate that while geosynthetic reinforcement improves the stability, steeper slopes (35°) inherently exhibit a reduced load-bearing capacity due to their higher susceptibility instability.

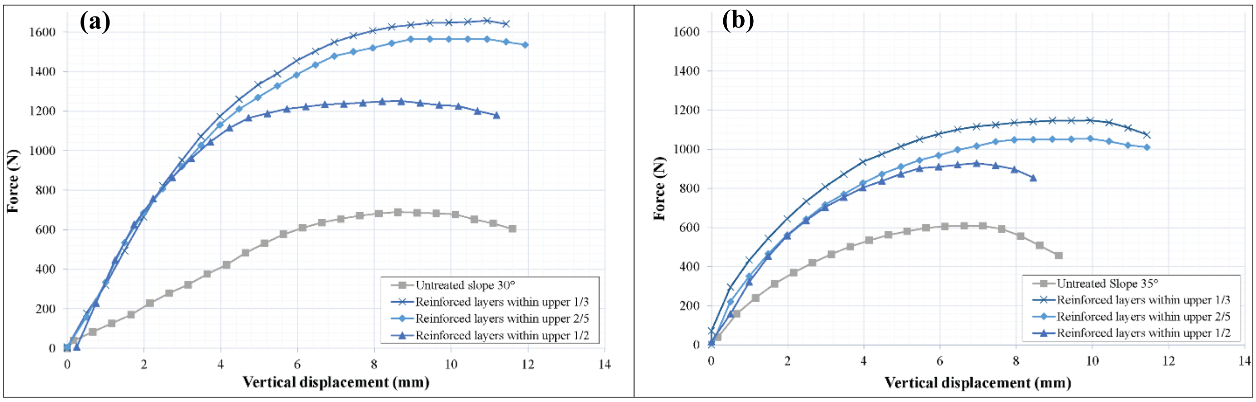

Figure 13. Maximum load supported under untreated and reinforced conditions for (a) 30° and (b) 35° slopes.

4.2. Displacement fields in untreated and reinforced slopes

Using the DID method, untreated 30° slopes exhibited displacements ranging from 4.05 mm to 4.80 mm at failure loads between 679 N and 736 N. In contrast, reinforced slopes demonstrated significantly lower displacements under higher loads. For instance, with one-half spacing, a load of 1250 N resulted in a displacement of 6.2 mm, which increased to 7.4 mm at a load of 1700 N for reinforcement layers distributed within the upper one-third (1/3).

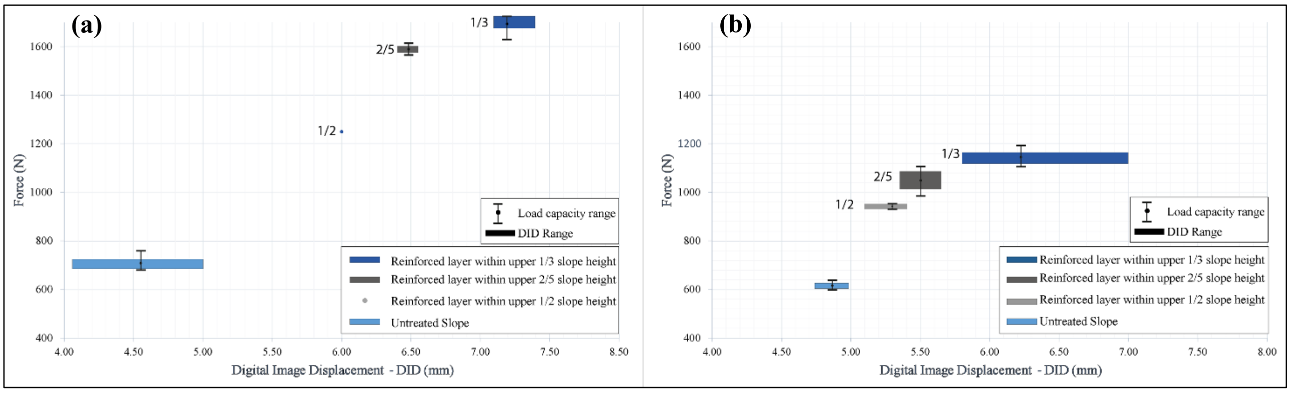

Figure 14. Displacement versus force for untreated and reinforced conditions for(a) Slope angle = 30° (b) Slope angle = 35°.

For 35° slopes, the displacement behavior followed similar trends, with reinforced slopes consistently showing reduced displacements compared to untreated ones (Figure 14). These results emphasize that geosynthetic reinforcement increases the load-bearing capacity and significantly improves the slope stability by minimizing the displacement.

4.3. Failure shapes in untreated and reinforced slopes

Failure shapes in untreated and reinforced slopes were examined using DID images focused on circular and logarithmic spiral shapes (Figure 15), which are the most recognized and commonly used. The analysis revealed that logarithmic spiral shapes most accurately represent the rupture surfaces, as described by parametric equations $x(\theta) = ae^{b\theta}\cos\theta$ and $y(\theta) = ae^{b\theta}sin\theta$ [24]. For untreated slopes, the rupture surface was smaller and shallower, thus reflecting the lower load required for failure. In contrast, reinforced slopes exhibited larger and deeper rupture surfaces, thus indicating their enhanced ability to withstand higher loads before failure. This distinction between slope angles underscores the effectiveness of geosynthetic reinforcement in improving the slope stability and load-bearing capacity.

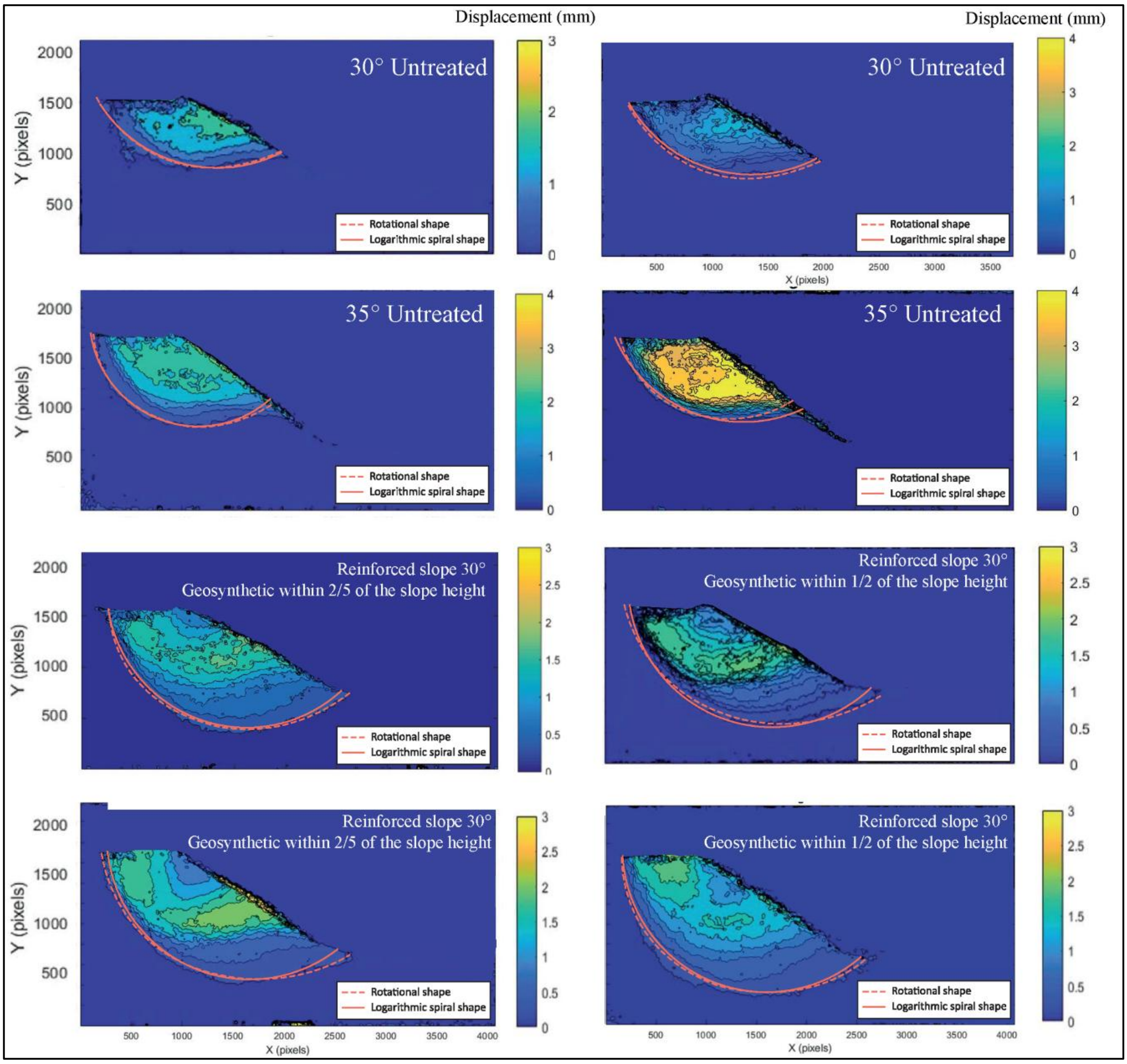

Figure 15. Fitting the circular and logarithmic spiral surfaces in the DID images representing the untreated and reinforced slope failure shapes.

4.4. Calculation of factor of safety (FS)

The application of geosynthetic reinforcement, particularly when layers were distributed within the upper one-third (1/3) of the slope height, resulted in a massive increase in stability across both tested geometries. For 30° slopes, the FS increased from 1.2 to 3.12, representing a 160% stability gain; similarly, 35° slopes saw an FS improvement from 1.02 to 2.67, representing a 162% increase (Figure 16).

While these gains are significant, the data confirms that steeper slopes (35°) remain inherently riskier than 30° slopes, thus supporting lower maximum loads and maintaining lower FS values even when reinforced. This observation aligns with the standard geotechnical theory, which identifies the slope angle as a primary determinant of stability, as geometries near the soil's 37° angle of repose are naturally closer to a critical state.

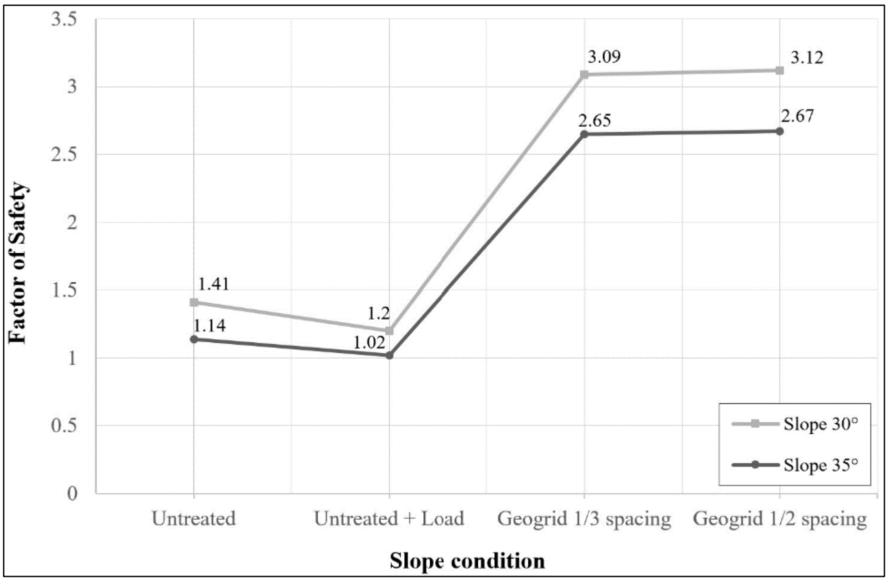

Figure 16. FS variation with untreated and reinforced conditions for 30° and 35°.

4.5. Evidence of performance enhancement and displacement tolerance

Evidence from 41 experiments confirms that geosynthetic reinforcement when layers were distributed within the upper one-third (1/3) of the slope height significantly transforms the slope stability by shifting failure mechanisms from brittle to ductile, thereby expanding the displacement tolerance of the slope [25]. This transformation addresses the apparent contradiction in the data: while reinforcement reduces the displacement due to identical loading conditions compared to the untreated slope, it allows the system to accomodate a greater total displacement before an ultimate collapse occurs.

As summarized in Tables 4 and 5, reinforced 30° slopes achieved a 143% increase in the load-bearing capacity and a 160% stability gain, while 35° slopes demonstrated a 95% capacity increase and a 162% stability gain.

Performance at Identical Loads: The inclusion of geosynthetics minimizes the internal soil movement and optimizes the load distribution, which results in a lower displacement for any given force compared to the untreated baseline.

Performance at Failure: Because the reinforced mass can sustain significantly higher loads (e.g., 1700 N vs. 700 N), it reaches a higher total max displacement (7.4 mm vs. 4.8 mm) without sudden collapse.

These trends are supported by the dual-axis error bars in Figure 14, which demonstrate high repeatability across the “Range of Force” and “Range of DID”. The displacement tolerance increased by up to 80% for 30° slopes and 48% for 35° slopes, thus confirming that the reinforced system is not only stronger but more resilient. This behavior was further validated by PLAXIS 3D numerical simulations, which successfully captured the ductile deformation patterns observed in the laboratory testing box.

Table 4. Comparative performance and statistical enhancement metrics for 30° slopes (Untreated vs. Reinforcement).

Metric	Untreated (30°)	Reinforcement within 1/3 Slope Height	Enhancement
Avg. Max Load	700 N	1700 N	~143% Load-bearing capacity increase
Factor of Safety	1.2	3.12	160% Stability Gain
Displacement	4.05–4.80 mm	7.1–7.4 mm	75% to +80 % tolerance

Table 5. Comparative performance and statistical enhancement metrics for 35° slopes slopes (Untreated vs. Reinforcement).

Metric	Untreated (30°)	Reinforcement within 1/3 Slope Height	Enhancement
Avg. Max Load	600 N	1171 N	95.17% Load-bearing capacity increase
Factor of Safety	1.02	2.67	162% Stability Gain
Displacement	4.75–4.98 mm	5.8–7.0 mm	22% to 48 % tolerance

4.6. Compaction effect on loading support

Compaction significantly influences the soil strength, with variations leading to different compression curves. This study examined 30° and 35° slopes under untreated and reinforced conditions, thus ensuring consistent compaction across three layers, each compacted with 24 hammer tamps to produce comparable compression curves (Figures 7 and 10).

However, preliminary tests were conducted to assess the effect of varying compaction on the curve behavior. On the 30° slope, applying 10 tamps resulted in a continuous increase in the compression curve without reaching a peak, thus indicating loose soil. In contrast, using 20 tamps per layer produced shorter curves and lower maximum loads compared with 24 tamps, and using 30 tamps per layer produced higher curves and higher maximum loads compared with 24 tamps, thus demonstrating the importance of compaction in the slope’s load-bearing capacity.

5. Conclusions

1. Geosynthetic Reinforcement Effectiveness: Geosynthetic reinforcement significantly transforms the mechanical behavior of sandy slopes by shifting the failure mechanism from a brittle to a ductile state. This shift allows reinforced slopes to accommodate greater total deformations while sustaining much higher loads—reaching 1700 N for 30° slopes and 1171 N for 35° slopes, representing a 143% and 95.17% increase in the load-bearing capacity.

2. Reduced Displacement with Reinforcement: Reinforced slopes exhibit lower displacements under identical loads than untreated slopes. Moreover, distributing reinforcement layers within smaller zones of the slope height further minimizes displacement, with the configuration in the upper one-third (1/3) proving the most effective design criterion to enhance the slope stability and optimize the load distribution. These findings underscore the critical role of reinforcement placement in maximizing slope performance.
3. Verification of Displacement Methods: The study successfully applied the novel DID method, which, unlike previous techniques, offers pixel-level sensitivity crucial to track the earliest stages of deformation and progressive failure. This consistency between DID and numerical PLAXIS 3D simulations validates the reliability of the DID technique for future slope monitoring and analyses.
4. Rupture Surface Characteristics: Reinforced slopes exhibit deeper and more pronounced rupture surfaces than untreated slopes. The finding that logarithmic spiral shapes provide the best fit for these surfaces confirms a predictive model for engineers. Crucially, the mobilization of these shapes was possible because the internal friction angle of the sand (37°) was notably higher than the soil–polycarbonate interface friction (21°). This ensured that internal failure mechanisms, governed by the soil's shear strength and geosynthetic reinforcement, were the dominant drivers of slope behavior, rather than artificial boundary effects from the container walls.
5. The FS Improvement: Geosynthetic reinforcement substantially increases the safety factor. For 30° slopes, the FS improves over 3 with reinforcement, compared to just 1.2 for untreated slopes. This significant increase validates geosynthetics as a primary risk mitigation technique in geotechnical engineering. Although 35° slopes also show an improvement in the safety factor, the values remain lower than those for 30° slopes, thus emphasizing the more significant challenges posed by steeper slopes in terms of stability.
6. Impact of Compaction: Consistent compaction across soil layers significantly enhances the slope performance, thus increasing the maximum loads supported. Therefore, proper soil compaction is a critical design parameter and operational step to optimize the slope stability, thus highlighting the need for thorough soil preparation in reinforced slope designs.
7. Comprehensive Considerations for Slope Stability: The study confirms that geosynthetic reinforcement improves the slope stability. However, additional factors such as the slope geometry and compaction can significantly influence the overall stability of the slope. By considering all these factors, a holistic approach to slope design is crucial to achieve optimal results.

Use of AI tools declaration

The authors declare they have not used Artificial Intelligence (AI) tools in the creation of this article.

Acknowledgments

The authors greatly appreciate the support provided by the mineral and mechanical engineering departments at the New Mexico Institute of Mining and Technology. This work is reprinted with permission from my New Mexico Institute of Mining and Technology thesis. During the preparation of this study, the authors used Mathematica software, version 13.3, Matlab version R2024b, Plaxis3D, version 2024.01 and Slide2D, version 6.0 for the purposes of optical displacement analysis, visualization and scale correction, numeral simulation, and results verification, and FS calculation

respectively. The authors have reviewed and edited the output and take full responsibility for the content of this publication.

Conflicts of interest

The authors declare no conflicts of interest.

References

1. Fleming R, Taylor F (1980) Estimating the costs of landslide damage in the United States. *US Department of the Interior, Geological Survey Circular 832*.
2. Schuster R, Fleming R (1986) Economic losses and fatalities due to landslide. *Environ Eng Geosci* xxiii: 11–28. https://doi.org/10.2113/gseegeosci.xxiii.1.11
3. Leroueil S (2001) Natural slopes and cuts: movement and failure mechanisms. *Géotechnique* 51: 197–243. https://doi.org/10.1680/geot.2001.51.3.197
4. Gee N (2024) Case study: Buffalo creek dam (West Virginia, 1972). Lessons learned from dam incidents and failures.
5. Plainly Difficult (2020) A brief history of: the Baia Mare dam disaster (short documentary).
6. The New York Times (2019) A tidal wave of mud. The New York times world.
7. Rotaru A, Bejan F (2024) Modelling of critical slip surface geometry for sustainable slope stability analysis. *Knowledge Transfer in the Sustainable Rehabilitation and Risk Management of the Built Environment*. know-re-built 2021. Springer series in geomechanics and geoengineering, Springer, Cham, 3–14. https://doi.org/10.1007/978-3-031-43455-6_1
8. Spencer E (1969) Circular and logarithmic spiral slip surfaces. *J Soil Mech Found Div* 95: 227–234. https://doi.org/10.1061/JSFEAQ.0001219
9. Yang KB, Zhu YP (2023) Searching for sliding surfaces in multi-level loess slopes based on the brachistochrone. *Sci Rep* 13: 6496. https://doi.org/10.1038/s41598-023-33559-4
10. Celestino TB, Duncan JM (1981) Simplified search for noncircular slip surface. *Proceedings of the 10th International Conference on SMFE*, Stockholm, Sweden, 391–394.
11. Li KS, White W (1987) Rapid evaluation of the critical slip surface in slope stability problems. *Int J Numer Anal Methods Geomech* 11: 449–473. https://doi.org/10.1002/nag.1610110503
12. Bäck T (1996) *Evolutionary algorithms in theory and practice: evolution strategies, evolutionary programming, genetic algorithms*, Oxford University Press.
13. Sengupta A, Upadhyay A (2009) Locating the critical failure surface in a slope stability analysis by genetic algorithm. *Appl Soft Comput* 9: 387–392. https://doi.org/10.1016/j.asoc.2008.04.015
14. Juang CH, Gong W, Martin JR, et al. (2018) Model selection in geological and geotechnical engineering in the face of uncertainty—Does a complex model always outperform a simple model? *Eng Geol* 242: 184–196. https://doi.org/10.1016/j.enggeo.2018.05.022
15. Kayadelen C, Önal TÖ, Altay G (2018) Experimental study on pull-out response of geogrid embedded in sand. *Measurement* 117: 390–396. https://doi.org/10.1016/j.measurement.2017.12.024
16. Wang J, Liu F, Wang P, et al. (2016) Particle size effects on coarse soil-geogrid interface response in cyclic and post-cyclic direct shear tests. *Geotext Geomembr* 44: 854–861. https://doi.org/10.1016/j.geotexmem.2016.06.011

17. Liu CN, Ho YH, Huang JW (2009) Large scale direct shear tests of soil/PET-yarn geogrid interfaces. *Geotext Geomembr* 27: 19–30. https://doi.org/10.1016/j.geotexmem.2008.03.002
18. Greco VR (1996) Efficient monte carlo technique for locating critical slip surface. *J Geotech Eng* 122: 517–525. https://doi.org/10.1061/(ASCE)0733-9410(1996)122:7(517)
19. Abdi MR, Mirzaeifar H (2017) Experimental and PIV evaluation of grain size and distribution on soil–geogrid interactions in pullout test. *Soils Found* 57: 1045–1058. https://doi.org/10.1016/j.sandf.2017.08.030
20. Mirzaeifar H, Hatami K, Reza Abdi M (2022) Pullout testing and Particle Image Velocimetry (PIV) analysis of geogrid reinforcement embedded in granular. *Geotext Geomembr* 50: 1083–1109. https://doi.org/10.1016/j.geotexmem.2022.06.008
21. ASCE AH, Guler M, ASCE TB (2004) Use of image analysis in determination of strain distribution during geosynthetic tensile testing. *J Comput Civ Eng* 18. https://doi.org/10.1061/(ASCE)0887-3801(2004)18:1(65)
22. Pan B, Quian K, Xie H, et al. (2009) Two-dimensional digital image correlation for in-plane displacement and strain measurement: a review. *Meas Sci Technol* 20: 2009. https://doi.org/10.1088/0957-0233/20/6/062001
23. Wu Y, Yang J, Zhang Y, et al. (2024) Combination of digital image processing and random generation in modeling soil-rock mixture slopes for post-failure analyses by material point method. *Comput Geotech* 165: 105866. https://doi.org/10.1016/j.compgeo.2023.105886
24. Wolfram Language Documentation, Mathematica—Wolfram, ImageDisplacements.
25. Araujo G (2024) Experimental and numerical studies of displacement fields anf failure mechanisms in unthreated and reinforced slopes uding digital image displacement (DID). *New Mexico Institute of Mining and Technology, Socorro, New Mexico*.